9 (2024) 100025

Contents lists available at ScienceDirect

IPEM-Translation

journal homepage: www.elsevier.com/locate/ipemt

Towards clinical translation of 7 Tesla MRI in the human brain

Graeme A. Keith [a,*], Rosemary A. Woodward [b], Tracey Hopkins [b], Sarah Allwood-Spiers [c,a], Jon Trinder [a], Keith W. Muir [a,d], David A. Porter [a], Natasha E. Fullerton [e,a]

[a] Imaging Centre of Excellence, University of Glasgow, Glasgow, Scotland, UK
[b] Glasgow Clinical Research Imaging Facility, NHS Greater Glasgow and Clyde, Glasgow, Scotland, UK
[c] Dept. Of Medical Physics, Queen Elizabeth University Hospital, NHS Greater Glasgow and Clyde, Glasgow, Scotland, UK
[d] Dept. of Neurology, Institute of Neurological Sciences, Queen Elizabeth University Hospital, NHS Greater Glasgow and Clyde, Glasgow, Scotland, UK
[e] Dept. of Neuroradiology, Institute of Neurological Sciences, Queen Elizabeth University Hospital, NHS Greater Glasgow and Clyde, Glasgow, Scotland, UK

ARTICLE INFO

Keywords:
Clinical MRI
7 tesla
Ultra-high field
MR spectroscopy

ABSTRACT

Clinical translation of 7 tesla (T) MRI of the brain promises high image quality and potentially improved clinical diagnosis for patients compared to current standard lower field-strength MRI at 1.5 and 3T.

Here we describe how physics principles underlying ultra-high field (UHF) strength MRI affect 7T image quality, and how these can be exploited to translate 7T brain imaging into clinical practice. UHF MRI profits from higher inherent signal-to-noise ratio (SNR) and a resultant increase in achievable spatial resolution or acceleration factors; increase in sensitivity to magnetic susceptibility differences and a higher amplitude of the Blood Oxygen Level Dependent (BOLD) signal; increase in longitudinal relaxation time; and increased frequency dispersion and spectral resolution in MR spectroscopy.

Examples are presented of different brain pathologies, which are better illustrated on 7T compared to lower field strength by applying sequences and imaging techniques that exploit these intrinsic strengths of 7T MRI. This includes imaging of various vascular pathologies, epilepsy and brain tumours.

Introduction

Ultra-high Field (UHF) Magnetic Resonance Imaging (MRI), such as at 7 tesla (T), is a powerful tool for exploring aspects of brain function and the mechanisms underlying disease. The greater static magnetic field strength (B_0), when compared to a 1.5 and 3T field strength more commonly found in clinical and research scanners, means significantly higher inherent signal-to-noise ratio (SNR) [1]. This has been shown to be in the order of $SNR \propto B_0^{1.65}$, using standard experimental setups and taking changes in relaxation time and flip angle homogeneity into account [2]. This supralinear SNR increase with higher field strength allows for the acquisition of images of far higher resolution than can be achieved on standard clinical systems; permitting the visualisation of smaller structures and vessels in the brain in far greater detail than was previously possible. In addition, higher acceleration factors can be applied in image acquisition, where the majority of methods, such as the phased array [3] parallel imaging techniques SENSitivity Encoding (SENSE) [4] and GeneRalized Autocalibrating Partially Parallel Acquisitions (GRAPPA) [5] or undersampling for compressed sensing reconstruction [6], carry some SNR penalty.

In addition to an increase in SNR, imaging at higher values of B_0 brings increased sensitivity to differences in magnetic susceptibility (χ) between tissue types [7]. This sensitivity can be exploited with the acquisition of T_2*-weighted gradient echo (GRE) magnitude and phase images, with short echo times (TE), to create high resolution Susceptibility-Weighted Images (SWI) [8] showing the venous system of the brain in great detail. This is achieved by the multiplication of the magnitude image with a phase mask and can additionally be visualised across the whole acquisition slab with a Minimum Intensity Projection (minIP). As compounds, such as haemoglobin, ferritin, and haemosiderin are paramagnetic relative to the functional brain tissue, signal in voxels containing these compunds will undergo a phase shift [9], which allows these to be delineated in SWI.

The increase in T_2* dephasing, due to local B_0 field inhomogeneities, driven by the same sensitivity to susceptibility differences exploited in SWI, also leads to a higher amplitude of the Blood Oxygen Level Dependent (BOLD) signal [10] used to measure brain activation in functional MRI (fMRI) studies. BOLD imaging at 7T also benefits from

* Corresponding author.
E-mail address: graeme.keith@glasgow.ac.uk (G.A. Keith).

https://doi.org/10.1016/j.ipemt.2024.100025
Received 16 June 2023; Received in revised form 29 February 2024; Accepted 18 March 2024
Available online 21 March 2024

greater specificity and localisation of signals, due to the increased contribution from the microvasculature relative to larger vessels [11]. With these advantages, and the higher resolution imaging made possible by the increase in SNR, 7T fMRI can be used to measure the BOLD signal, relying on changes in cerebral blood flow (CBF) and volume (CBV), in distinct layers of the cortex [12]. This not only allows researchers to investigate neuronal feedback and feedforward mechanisms, for instance in the visual cortex, in a research context, but also facilitates clinical fMRI for functional mapping of eloquent cortex in relationship to tumours and epileptogenic foci [13].

While T_2* values of brain tissue decrease with higher field strength due to greater dephasing, T_1 values tend to increase, as the higher resonance frequency diverges from the frequencies for molecular motion for bound protons. This increase in longitudinal relaxation time can be utilised to improve suppression of unwanted signal. An example of this is the endogenous-contrast Time-of-Flight Magnetic Resonance Angiography (ToF-MRA) [14] technique for imaging of the arterial system of the brain. In ToF-MRA, the signal from tissue in the imaging slab is saturated, such that it has a low level of steady-state magnetisation. The inflowing blood arriving in the region has a high initial magnetisation, leading to a flow-related enhancement of blood signal, which contrasts strongly with the saturated signal of the background tissue. This shows clearly the bright vessels against a dark background, frequently even better seen looking at an imaging slab with a Maximum Intensity Projection (MIP).

In addition to the discussed MR imaging techniques, Magnetic Resonance Spectroscopy (MRS) at 7T also promises advantage over lower field strength. As well as the increase in SNR, increased frequency dispersion at 7T [15] leads to greater spectral resolution. This means that metabolite resonances, which overlap at lower field strengths, become separated and easier to resolve at 7T [16,17]. Unfortunately, this frequency dispersion also leads to greater Chemical Shift Displacement Error (CSDE) with standard techniques, such as Point-RESolved Spectroscopy (PRESS). As a result, localisation of metabolite signals could be incorrect due to use of the same bandwidth of radiofrequency (RF) pulse with greater frequency difference between resonances. This can be overcome with the use of advanced techniques, such as the Semi-adiabatic Localization by Adiabatic SElective Refocusing (sLASER) [18] sequence, which employs pairs of amplitude- and frequency-modulated adiabatic RF inversion pulses [19] in order to be more robust to CSDE. Furthermore, the J-coupling of spins is independent of field strength, which, along with the greater frequency dispersion described, means the effect of J-coupling at 7T is weaker than at lower field strengths. It has been reported that up to 17 metabolites can be robustly measured at 7T using advanced techniques, such as sLASER, compared with 12 metabolites using standard methods at 3T [15]. This makes MRS at 7T a powerful technique for the investigation of brain tissue metabolism in a range of neurological conditions.

Imaging at 7T does however have some additional challenges when compared with lower field strengths. The Specific Absorption Rate (SAR), which represents the amount of RF power deposited in tissue during imaging, scales with the square of B_0 [20]. This deposited energy raises tissue temperature and can lead to patient injury if not strictly controlled. In addition, the proportionality of resonance frequency with field strength, described by the Larmor equation, means that the wavelength of RF energy applied at higher fields for the excitation of ^{1}H spins decreases linearly. At 7T, this wavelength is in the order of 12 cm [21] in tissue. As this is less than the average human skull and brain diameter, a pattern of constructive and destructive interference occurs in imaging, which results in inhomogeneity of the actual flip angle achieved across a slice, leading to bright and dark patches in images. Both of these issues can be addressed by the application of parallel transmit techniques [22,23], whereby RF coils with multiple transmit elements [24,25] are driven independently to create a more homogeneous RF field and improve image quality. Application of these advanced methods, however, is beyond the scope of this translational study and remains an active area of pulse sequence and RF hardware development.

In this work, we present early translational clinical data acquired on our 7T system in patients with various pathologies, including brain tumours, cerebrovascular conditions and epilepsy. We show some of the benefits of applying UHF imaging in clinical research studies and some possible future clinical indications.

Methods

As part of a clinical imaging study, patients with a variety of neurological conditions were scanned under Research Ethics Committee approval (REC reference: 18/WS/0141), to compare 7T with lower field-strength MRI. Pathologies scanned included cerebrovascular conditions, brain tumours, epilepsy, neurodegenerative and neuroinflammatory disease. All scans were performed on a 7T MAGNETOM Terra scanner (Siemens Healthineers AG, Erlangen, Germany) with a commercial single-channel transmit, 32-channel receive RF head coil (Nova Medical, Wilmington, MA, USA). Scan protocols varied and were tailored to the underlying clinical question and pathology.

Pulse sequences applied included a T_1-weighted, two readout variant of the Magnetisation-Prepared RApid Gradient Echo sequence (MP2RAGE [26]). This differs from the standard MPRAGE [27] sequence by the acquisition of images at two values of inversion time (TI) following a non-selective inversion pulse. The first of these has a strong T_1-weighting and the second, acquired at a longer TI, has greater proton density weighting. These two images are then combined with a simple expression, where the product of the two images is divided by the sum of squares, such that the resultant image is strongly T_1-weighted and robust to the influence of B_0 and B_1 inhomogeneities [26].

Also included in scan protocols were T_2-weighted Turbo Spin-Echo (TSE), FLuid Attenuated Inversion Recovery (FLAIR), SWI, ToF-MRA, REadout Segmentation Of Long Variable Echo Diffusion Weighted Imaging (RESOLVE-DWI) [28] and BOLD-Echo Planar Imaging (EPI) for fMRI.

In some patient subgroups, sLASER MRS was also acquired, for which VAriable Pulse power and Optimized Relaxation delays (VAPOR) water suppression [29] and 3D Outer-Volume Suppression (OVS) were used to suppress unwanted signal from water and from outside the voxel of interest, respectively. Unsuppressed water spectra were also acquired with and without applied magnetic field gradients, for the purpose of metabolite quantification by water scaling and eddy current correction. Fast, Automatic Shim Technique using Echo-planar Signal readouT for Mapping Along Projections, (FAST(EST)MAP) B_0 shimming [30] was used prior to the acquisition to achieve static magnetic field homogeneity in the voxel of interest. An unsuppressed water peak linewidth of $\leq$13 Hz was deemed acceptable according to consensus recommendations for 7T [31]. Corrections were performed for eddy current effects, and frequency and phase contributions using the Magnetic Resonance Spectral Processing and Analysis package (MRspa, Deelchand, University of Minnesota) in MATLAB (R2018b, Mathworks, Natick, MA) and the resulting spectra were then fitted for quantitative results in LCModel [32].

For functional acquisitions, a task-based fMRI was performed, presenting a motor paradigm comprising a block design with alternating baseline and active blocks of 30 s duration while acquiring BOLD-EPI images. Functional MRI data processing was carried out using FEAT (FMRI Expert Analysis Tool) version 6.00. The following pre-statistics processing was applied; motion correction using MCFLIRT [33]; non-brain removal using BET [34]; spatial smoothing using a Gaussian kernel of FWHM 5 mm; grand-mean intensity normalisation of the entire 4D dataset by a single multiplicative factor; high-pass temporal filtering (Gaussian-weighted least-squares straight line fitting, with sigma=45.0 s). Time-series statistical analysis was carried out using FILM with local autocorrelation correction [35]. Z (Gaussianised T/F) statistic images were thresholded using clusters determined by $Z > 3.5$ and a (corrected)

cluster significance threshold of $P = 0.05$ [36].

All relevant MRI/MRS pulse sequence parameters for presented 7T data are recorded in Table 1.

Results

7T imaging results are presented for patients with different vascular conditions, epilepsy and brain tumours, along with MRS data from a glial tumour with healthy tissue comparison.

Fig. 1 shows (a) 7T SWI data from a middle-aged male patient with Cerebral Amyloid Angiopathy (CAA) and (b) zoomed aspects of (a) demonstrating sulcal subarachnoid haemosiderin deposition. A 3T SWI in the same patient is presented in Fig. 1(c) for comparison.

Fig. 2 shows ToF-MRA MIP data of the Circle of Willis (CoW) in a young female patient with intracranial vasculopathy with occlusion and neovascularisation [37] showing a slab of thick slab width (SW) of 39 mm encompassing the whole field-of-view scanned at (a) 7T and (b) 3T. Further focused MIP images of the CoW with 10 mm SW at (c) 7T and (d) 3T are presented, with the slab angled to ensure adequate cover of the proximal Circle of Willis. This shows the excellent depiction at 7T.of areas of narrowing affecting the proximal CoW.

Fig. 3 shows 7T imaging from a patient with a left frontal intrinsic brain tumour (oligodendroglioma), including (a) a T_2-weighted TSE, (b) T_2-FLAIR, and (c) SWI; and corresponding 3T imaging in (d)-(f).

Data from five different epilepsy patients is presented in Fig. 4. In the first patient, a clear epileptogenic focus (grey matter heterotopia) is demonstrated at 7T in both (a) a T_2-TSE and (b) a single inversion time image from a T_1-weighted MP2RAGE acquisition. A coronal T_2-TSE sequence (c) obtained from a patient (patient 2) with epilepsy shows bilaterally normal hippocampi. In contrast, 7T T_2-TSE (d) in a patient with temporal lobe epilepsy (patient 3) shows right hippocampal volume loss, loss of normal hippocampal architecture, and high T2-weighted signal, in keeping with right mesial temporal sclerosis (MTS). Also presented are, (e) a 3T T_2-FLAIR and (f) a 7T T_2-FLAIR image from a fourth patient. 3T imaging demonstrates the epileptogenic focus, a calcified lesion in the left fusiform gyrus, which is not clearly appreciable on the 7T imaging. Likewise, (g) a 3T T_2-FLAIR image for patient 5, shows subtle prominence of the left amygdala with some signal change and blurring of grey-white matter junction, in keeping with temporal lobe epilepsy with amygdala enlargement, again not clearly appreciable on (h) a 7T T_2-FLAIR.

Fig. 5 presents 7T data from a patient with a right frontal anaplastic oligodendroglioma. Sequences presented include (a) T_2-TSE, (b) T_2-FLAIR, (c) SWI, and (d) RESOLVE-DWI. A (e) high resolution spectrum, acquired with the sLASER sequence, with the voxel sampled placed over the right frontal tumour volume indicated in (a), along with (f) a spectrum acquired in a healthy volunteer for comparison. In addition, (g) task-based left hand motor paradigm fMRI results are shown. The fMRI activation was co-registered with structural MP2RAGE sequences, for pre-operative mapping of eloquent brain areas in relationship to the tumour.

Discussion

In this work, we illustrate 7T imaging in a range of clinical conditions including brain tumours, epilepsy and intracranial arterial disease. These include high resolution T_1- and T_2- weighted structural imaging with MP2RAGE and T_2-TSE, as well as T_2-FLAIR, for exquisitely detailed anatomical images of the brain. High-resolution vascular imaging with ToF-MRA and SWI allowed for detailed visualisation of the arterial and venous systems respectively, with further SWI used for detection of blood products and calcification. Additionally, RESOLVE-DWI, motor paradigm functional imaging, and high spectral resolution MR spectroscopy with sLASER were applied. In some cases, 7T imaging is contrasted with 3T imaging from the same patient. All 3T images were acquired with standard clinical protocols on different 3T scanner setups corresponding to the patient's clinical pathway and thus represent a clinically valuable, informative comparison.

A clear strength of imaging at 7T is in the application of vascular imaging methods to visualise the vessels in neuropathology, and improve visualisation of calcification, micro-haemorrhages and haemosiderin staining. This is demonstrated in the SWI images presented in Fig. 1, where the higher resolution images available, due to increased SNR, offer greater anatomical detail of grey-white matter junction and cortex. This, along with the greater sensitivity to differences in susceptibility, allows for the visualisation of sulcal subarachnoid haemosiderin deposition, as highlighted in Fig. 1 by the blue arrows. The power of SW imaging at 7T is also demonstrated in the tumour imaging in Figs. 3 and 5(c), showing in detail the underlying microvascular architecture of glial tumours and microhaemorrhages and microcalcification, highlighted in Fig. 3 by the blue arrows. These features are more difficult to appreciate on the presented 3T imaging.

High-resolution images of the arterial system at 7T are also achievable without intravenous contrast agents, by using the time-of-flight MR angiography method. This is demonstrated in Fig. 2, where 7T and 3T ToF-MRA images are presented for a patient with intracranial vasculopathy with occlusion and neovascularisation. The 7T images demonstrate narrowing and irregularities of the M1 segment of the MCA and the A1 segment of the ACA, which were more difficult to appreciate on 3T MRI. In addition, early neovascularisation can be seen. This is enhanced by improved background suppression of the signal arising from the static tissue present in the imaging slab. This allows for greater contrast with the flow-enhanced signal from the inflowing blood. The quality and vascular detail of 3D ToF images of the Circle of Willis achieved at 7T, including visualisation of distal branch vessels of the Circle of Willis, rivals those beforehand only seen on interventional digital subtraction angiography, which can be associated with potential discomfort and complications for the patient.

The benefits of higher-resolution imaging, arising from the scaling of SNR with field strength, are also shown in structural T_1- and T_2-weighted imaging. This is well demonstrated in the anatomical imaging for the two tumour patients, presented in Figs. 3 and 5(a) and (b), which show T_2-weighted TSE and FLAIR imaging, respectively. The high

Table 1
Sequence parameters for 7T imaging and spectroscopy.

	TR/TE (ms)	Image resolution (mm^3)	Image matrix	Slices	Acceleration	BW/px (Hz)	Other	Acq. Time (mm:ss)
MP2RAGE	5000/1.94	0.8 × 0.8 × 0.8	320×320	208	GRAPPA 3	490	–	08:27
TSE	9000/58	0.4 × 0.4 × 3.0	512×384	39	GRAPPA 2	287	Turbo factor 9	03:38
FLAIR	12,820/59	0.5 × 0.5 × 3.0	448×336	39	GRAPPA 2	286	Turbo factor 9	04:31
SWI	21/14	0.2 × 0.2 × 1.5	896×728	72	GRAPPA 3	210	–	07:29
ToF	13/4.58	0.3 × 0.3 × 0.3	704×540	144	GRAPPA 3	203	–	06:44
RESOLVE-DWI	4890/58	1.0 × 1.0 × 3.0	224×224	34	GRAPPA 3	698	b-Value 0/1000 s/mm^2	03:42
sLASER	5000/30	20×17×20	–	–	–	6000 (spectral BW)	2048 complex points, 64 averages	06:10
BOLD-EPI	3000/20	2 × 2*2	111×111	75	GRAPPA 3	1860 (FE direction)	Echo train length 37, FA 75°	05:00

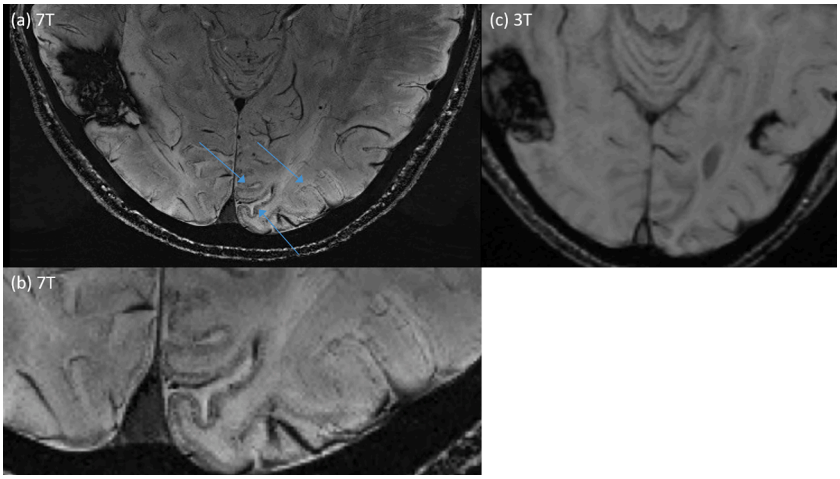

Fig. 1. (a) A 7T Susceptibility-Weighted Image of the occipital and posterior temporal lobes in a patient with cerebral amyloid angiopathy, along with (b) a zoomed-in image. Sulcal subarachnoid haemosiderin deposition (arrows) and anatomical detail of the cortex were demonstrated on 7T but not seen on (c) 3T SWI imaging.

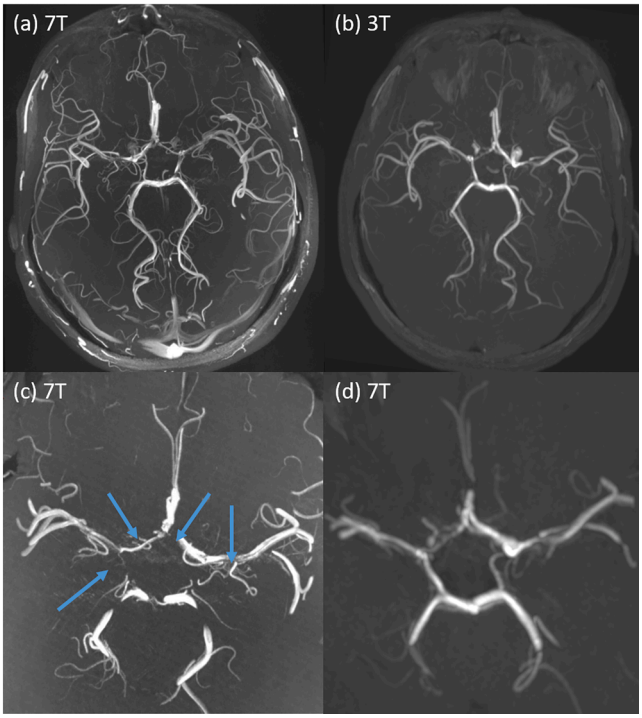

Fig. 2. (a) a 7T Time-of-flight MR angiogram (MRA), high slab width (39 mm) maximum intensity projection (MIP) demonstrating the anatomical detail of the Circle of Willis (CoW), including the M4 branch vessels of the middle cerebral arteries (MCAs); (b) a 3T MIP MRA of high slab thickness in the same patient, of lesser resolution with M4 branches poorly seen. Image (c) a 10 mm SW 7T MRA slab in the same patient focussed on and angled to cover the CoW optimally. This is demonstrating narrowing and irregularities of M1 segments of the MCAs and A1 segments of the anterior cerebral arteries (ACAs) (arrows) in a patient with vasculitis and Moyamoya syndrome. (d) 3T 10 mm SW MRA MIP slab in the same patient, of lesser resolution than the 7T imaging. The areas of narrowing and irregularity affecting the CoW are less well demonstrated.

spatial resolution and increase in Contrast-to-Noise Ratio (CNR) make it possible to see anatomical and structural details of the tumour matrix, not appreciable on lower resolution 3T imaging.

In the case of the first of the five epilepsy patients presented in Fig. 4, there is high lesional contrast demonstrated in the T_2-weighted TSE image in Fig. 4(a). This allows for strong visualisation of grey matter heterotopia, showing increased conspicuity of this migrational anomaly, a possible epileptogenic focus. This is also shown at the first inversion time from the MP2RAGE acquisition in Fig. 4(b), which shows high contrast between white matter and the grey matter lesion. Fig. 4(d) shows a T_2-TSE image of an epilepsy patient with right mesial temporal sclerosis (MTS), compared to an epilepsy patient with normal hippocampi in Fig. 4(c). The high resolution, SNR and CNR enables superb depiction of loss of normal anatomy, loss of hippocampal volume and high signal within the right hippocampal head in Fig. 4(d), reflecting MTS. Hippocampal layers can be appreciated with great anatomical detail in the normal hippocampi shown, secondary to the high resolution at 7T. By contrast, patients 4 and 5 show that, in some cases, 3T imaging can provide more clinical value than 7T. The 3T T_2-FLAIR in Fig. 4(e) clearly demonstrates the epileptogenic focus, a calcified lesion in the left fusiform gyrus. Due to the position of the lesion at the antero-inferior skull base, the corresponding 7T image (f) shows some local signal loss and poor contrast. Likewise, in patient 5, a subtle prominence of the left amygdala with some signal change and blurring of grey-white matter junction is better visualised in the 3T T_2-FLAIR (g). This is in keeping with temporal lobe epilepsy with associated amygdala enlargement. The images from patients 4 and 5 highlight the shortfalls and limitations of 7T imaging in some patients with pathology in close proximity to the skull base and in anterior or inferior temporal lobes.

In Fig. 5(i), a high-resolution sLASER spectrum was obtained from a voxel, marked in Fig. 5(a), placed over a right frontal lesion in a 65-year-old male patient, confirmed on pathology as an anaplastic oligodendroglioma. The structural imaging benefits from the increased SNR, resolution and sensitivity to magnetic susceptibility differences, providing exquisite detail of the heterogenous tumour with vascularity, blood products and calcification (Fig. 5(a–d)). The spectrum shows the expected reduction in total N-Acetyl Aspartate (tNAA) due to the death of neurons present in the tumorous tissue, and increase in choline (Cho) due to high membrane turnover. This results in a decrease in NAA/Cho and increase in Cho/Cr (Creatine) ratios. In addition, a clear lactate peak is visible in the lesional spectrum, as a characteristic doublet at 1.3 ppm. Lactate is not normally present in measurable quantities in healthy brain tissue, as seen in the healthy volunteer spectrum in Fig. 5(j). It is a product of anaerobic metabolism, due to the increased oxygen demand and necrosis of higher-grade tumours, such as the anaplastic oligodendroglioma in this case. There is also a measureable increase in glutamine, as previously observed in gliomas [38]. This would not be observable at lower field strengths due to the overlap of the glutamine peak with glutamate. This is caused by insufficient spectral resolution, such that the value of the Glx peak (a combination of signal from Gln-and Glu) has been observed to show no change relative to

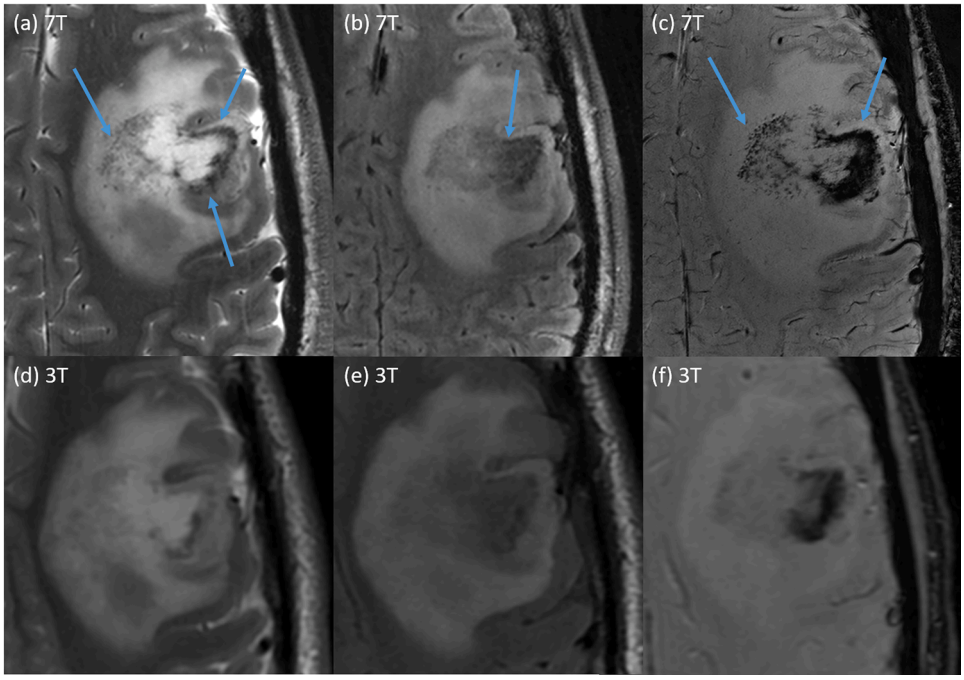

Fig. 3. Structural imaging of a patient with a left frontal brain tumour (oligodendroglioma) including (a) a 7T T_2-weighted TSE, (b) T_2-FLAIR, and (c) SWI and corresponding 3T (d) T_2-weighted TSE, (e) T_2-FLAIR, and (f) SWI. The 7T imaging is of higher resolution, SNR and CNR, demonstrating the tumour matrix exquisitely (arrows). The 7T imaging allows for high resolution showing tumour heterogeneity, calcification and blood products (arrows).

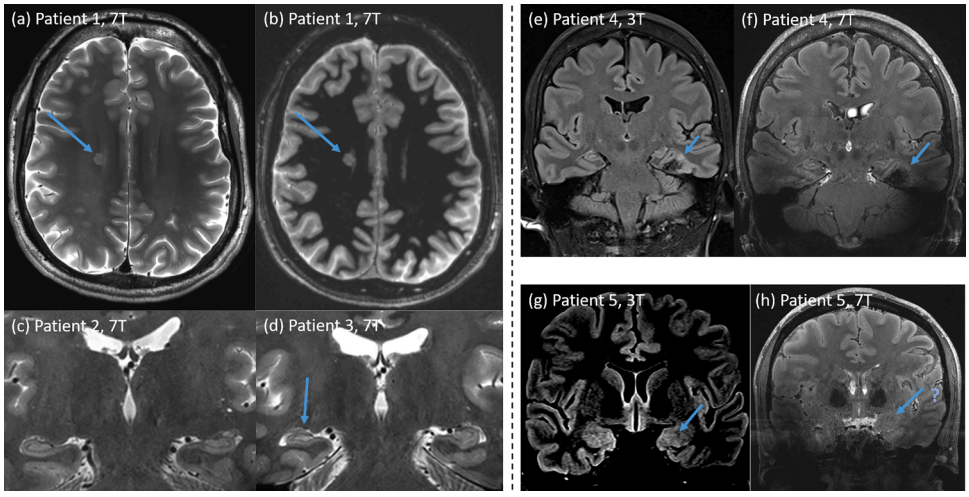

Fig. 4. Imaging from different patients with epilepsy. Patient 1; 7T MRI with (a) a T_2-weighted TSE and (b) a single inversion time image from a T_1-weighted MP2RAGE acquisition, showing an epileptogenic focus (grey matter heterotopia). Patient 2; 7T T_2-TSE image (c) of a normal hippocampus in an epilepsy patient suffering from temporal lobe epilepsy. Patient 3; in contrast, 7T T_2-TSE images (d) show abnormal hippocampal volume, architecture and signal in keeping with right mesial temporal sclerosis (MTS). Patient 4; (e) a 3T T_2-FLAIR and (f) a 7T T_2-FLAIR, with 3T imaging demonstrating the epileptogenic focus, a calcified lesion in the left fusiform gyrus. This is better visualised on 3T imaging due to the signal loss and inhomogeneity, and poor CNR and SNR at 7T. This is owing to the location of the lesion at the antero-inferior skull base. Patient 5; (g) a 3T T_2-FLAIR and (h) a 7T T_2-FLAIR, with the 3T imaging showing subtle prominence of the left amygdala with some signal change and blurring of grey-white matter junction. This is in keeping with temporal lobe epilepsy with associated amygdala enlargement, not clearly appreciable on the 7T imaging.

normal-appearing white matter [39].

Fig. 5(k) in the same tumour patient, shows haemodynamic activation on a left-hand movement motor paradigm in the right-hemispheric hand motor cortex. There is also haemodynamic activation in the supplementary motor area at the level of the superior frontal gyrus in the right hemisphere. This aids pre-operative planning, as well as planning for intra-operative stimulation by mapping the relationship of these eloquent cortical areas to the tumour. Functional MRI exploits the improved BOLD signal achieved at 7T secondary to neuronal-vascular-coupling. This presents early preliminary results with clinical fMRI at 7T to illustrate future clinical potential in pre-operative assessment and planning.

These examples of 7T clinical imaging and spectroscopy results show the potential benefits of UHF for greater structural, vascular and metabolic detail. Translating 7T MRI into clinical use requires understanding of the physical principles underlying UHF imaging. The intrinsic physical properties of UHF MRI allow tailoring of appropriate imaging protocols to the clinical question posed and to the underlying pathology.

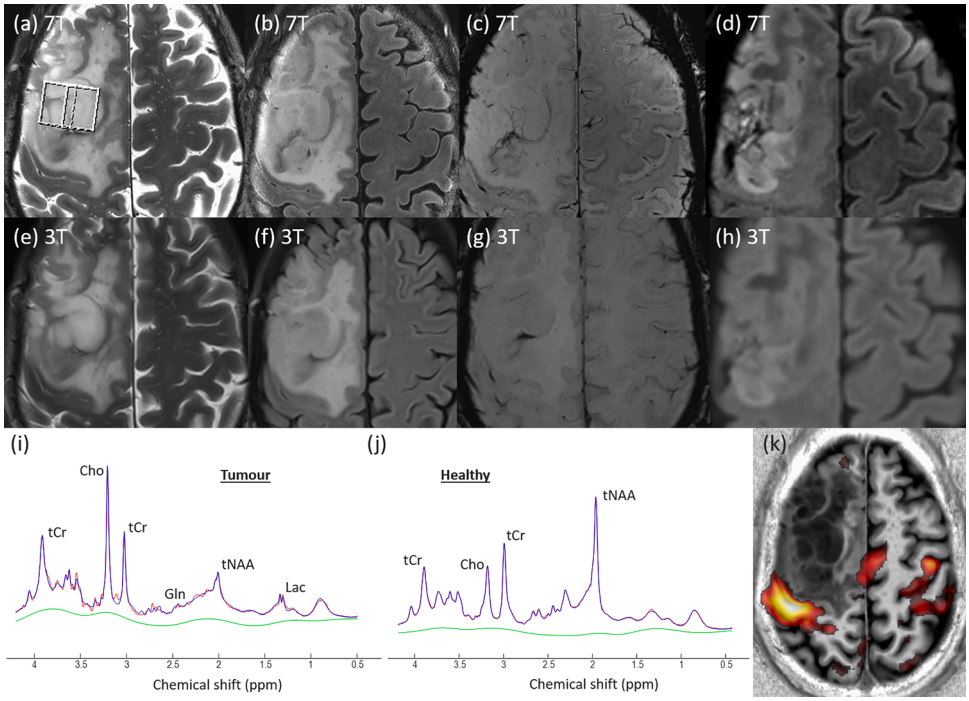

Fig. 5. 7T imaging in a patient with a right frontal anaplastic oligodendroglioma including, (a) T_2-TSE, (b) T_2 FLAIR, (c) SWI, and (d) RESOLVE-DWI. Corresponding 3T imaging, (e) T_2-TSE, (f) T_2 FLAIR, (g) SWI, and (h) RESOLVE-DWI, of lesser resolution than the 7T imaging, and hence showing less anatomical detail of the tumour matrix. Also presented are (i) an sLASER spectrum acquired in the tumour voxel marked in (a), (j) a spectrum from a healthy volunteer for comparison, and (k) haemodynamic activation on functional MRI during a left-hand block motor paradigm, with the raised BOLD signal co-registered with 3D T_1-weighted MP2RAGE images.

This opens the door for translation of 7T brain imaging into clinical practice. Understanding and knowledge of physics principles underlying UHF imaging is also critical in mitigating disadvantages of, and difficulties associated with 7T imaging. This ensures not only high image quality, but also, most importantly, patient safety. In addition to the increase in SAR and RF field inhomogeneity, 7T MRI suffers from greater B_0 field inhomogeneity, requiring extra orders of shim gradient [40] and specialist shimming methods to achieve a sufficiently homogenous field in the region of interest. The decrease in RF wavelength also means that the use of a body coil, built into the scanner bore, for RF transmission is impractical, so dedicated local transmit/receive coils for each body region of interest are required [21,24,25]. This, along with the larger magnet and multiple amplifiers required for parallel transmission, makes a 7T system a very expensive purchase.

In this work, we present examples of neurological conditions that may benefit from the intrinsic advantages of 7T MRI. These include increased SNR and resolution, increased T_1 longitudinal relaxation time, increased sensitivity to differences in magnetic susceptibility between tissues, increased BOLD signal, and increased spectral resolution. By successfully leveraging these properties we can open the door to precision medicine and diagnosis with the aid of 7T MRI.

Funding

None

Ethical approval

West of Scotland Research Ethics Committee (REC), REC reference: 18/WS/0141

CRediT authorship contribution statement

Graeme A. Keith: Writing – original draft, Software, Methodology, Formal analysis, Investigation, Visualization. **Rosemary A. Woodward:** Investigation, Methodology, Project administration. **Tracey Hopkins:** Investigation, Methodology, Project administration. **Sarah Allwood-Spiers:** Writing – review & editing, Methodology, Formal analysis, Investigation. **Jon Trinder:** Software, Resources. **Keith W. Muir:** Writing – review & editing, Conceptualization, Supervision. **David A. Porter:** Writing – review & editing, Methodology. **Natasha E. Fullerton:** Writing – original draft, Project administration, Methodology, Formal analysis, Investigation, Visualization, Conceptualization, Supervision.

Declaration of competing interest

None

Acknowledgements

None

References

[1] F. Schick, Whole-body MRI at high field: technical limits and clinical potential, Eur. Radiol. 15 (5) (2005) 946–959.
[2] R. Pohmann, O. Speck, K. Scheffler, Signal-to-noise ratio and MR tissue parameters in human brain imaging at 3, 7, and 9.4 tesla using current receive coil arrays, Magn. Reson. Med. 75 (2) (2016) 801–809.
[3] P.B. Roemer, W.A. Edelstein, C.E. Hayes, S.P. Souza, O.M. Mueller, The NMR phased array, Magn. Reson. Med. 16 (2) (1990) 192–225.
[4] K.P. Pruessmann, M. Weiger, M.B. Scheidegger, P. Boesiger, SENSE: sensitivity encoding for fast MRI, Magn. Reson. Med. 42 (5) (1999) 952–962.
[5] M.A. Griswold, P.M. Jakob, R.M. Heidemann, M. Nittka, V. Jellus, J. Wang, et al., Generalized autocalibrating partially parallel acquisitions (GRAPPA), Magn. Reson. Med. 47 (6) (2002) 1202–1210.
[6] M. Lustig, D. Donoho, J.M. Pauly, Sparse MRI: the application of compressed sensing for rapid MR imaging, Magn. Reson. Med. 58 (6) (2007) 1182–1195.
[7] J.H. Duyn, P. van Gelderen, T.Q. Li, J.A. de Zwart, A.P. Koretsky, M. Fukunaga, High-field MRI of brain cortical substructure based on signal phase, Proc. Natl. Acad. Sci. U. S. A. 104 (28) (2007) 11796–11801.

[8] E.M. Haacke, Y. Xu, Y.C. Cheng, J.R. Reichenbach, Susceptibility weighted imaging (SWI), Magn. Reson. Med. 52 (3) (2004) 612–618.
[9] F. Schweser, A. Deistung, B.W. Lehr, J.R. Reichenbach, Differentiation between diamagnetic and paramagnetic cerebral lesions based on magnetic susceptibility mapping, Med. Phys. 37 (10) (2010) 5165–5178.
[10] E. Yacoub, A. Shmuel, J. Pfeuffer, P.F. Van de Moortele, G. Adriany, P. Andersen, et al., Imaging brain function in humans at 7 Tesla, Magnet. Reson. Med. 45 (4) (2001) 588–594.
[11] T.Q. Duong, E. Yacoub, G. Adriany, X.P. Hu, K. Ugurbil, S.G. Kim, Microvascular BOLD contribution at 4 and 7 T in the human brain: gradient-echo and spin-echo fMRI with suppression of blood effects, Magnet. Reson. Med. 49 (6) (2003) 1019–1027.
[12] L. Muckli, F. De Martino, L. Vizioli, L.S. Petro, F.W. Smith, K. Ugurbil, et al., Contextual feedback to superficial layers of V1, Curr. Biol. 25 (20) (2015) 2690–2695.
[13] S. Tharin, A. Golby, Functional brain mapping and its applications to neurosurgery, Neurosurgery. 60 (4 Suppl 2) (2007) 185–201.
[14] J.T. Heverhagen, E. Bourekas, S. Sammet, M.V. Knopp, P. Schmalbrock, Time-of-flight magnetic resonance angiography at 7 Tesla, Invest. Radiol. 43 (8) (2008) 568–573.
[15] A. Henning, Proton and multinuclear magnetic resonance spectroscopy in the human brain at ultra-high field strength: a review, Neuroimage. 168 (2018) 181–198.
[16] I. Tkac, P. Andersen, G. Adriany, H. Merkle, K. Ugurbil, R. Gruetter, In vivo H-1 NMR spectroscopy of the human brain at 7 T, Magnet. Reson. Med. 46 (3) (2001) 451–456.
[17] I. Tkac, R. Gruetter, Methodology of H-1 NMR spectroscopy of the human brain at very high magnetic fields, Appl. Magn. Reson. 29 (1) (2005) 139–157.
[18] T.W. Scheenen, D.W. Klomp, J.P. Wijnen, A. Heerschap, Short echo time 1H-MRSI of the human brain at 3T with minimal chemical shift displacement errors using adiabatic refocusing pulses, Magn. Reson. Med. 59 (1) (2008) 1–6.
[19] A. Tannus, M. Garwood, Adiabatic pulses, NMR Biomed. 10 (8) (1997) 423–434.
[20] W. van der Zwaag, A. Schafer, J.P. Marques, R. Turner, R. Trampel, Recent applications of UHF-MRI in the study of human brain function and structure: a review, NMR Biomed. 29 (9) (2016) 1274–1288.
[21] J.T. Vaughan, M. Garwood, C.M. Collins, W. Liu, L. DelaBarre, G. Adriany, et al., 7T vs. 4T: RF power, homogeneity, and signal-to-noise comparison in head images, Magn. Reson. Med. 46 (1) (2001) 24–30.
[22] U. Katscher, P. Bornert, C. Leussler, J.S van den Brink, Transmit SENSE, Magn. Reson. Med. 49 (1) (2003) 144–150.
[23] Y. Zhu, Parallel excitation with an array of transmit coils, Magn. Reson. Med. 51 (4) (2004) 775–784.
[24] G. Adriany, P.F. Van de Moortele, F. Wiesinger, S. Moeller, J.P. Strupp, P. Andersen, et al., Transmit and receive transmission line arrays for 7 Tesla parallel imaging, Magn. Reson. Med. 53 (2) (2005) 434–445.
[25] S.N. Williams, S. Allwood-Spiers, P. McElhinney, G. Paterson, J. Herrler, P. Liebig, et al., A nested eight-channel transmit array with open-face concept for human brain imaging at 7 Tesla, Front. Phys-Lausanne 9 (2021).
[26] J.P. Marques, T. Kober, G. Krueger, W. van der Zwaag, P.F. Van de Moortele, R. Gruetter, MP2RAGE, a self bias-field corrected sequence for improved segmentation and T1-mapping at high field, Neuroimage 49 (2) (2010) 1271–1281.
[27] J.P. Mugler 3rd, J.R. Brookeman, Rapid three-dimensional T1-weighted MR imaging with the MP-RAGE sequence, J. Magn. Reson. Imaging 1 (5) (1991) 561–567.
[28] D.A. Porter, R.M. Heidemann, High resolution diffusion-weighted imaging using readout-segmented echo-planar imaging, parallel imaging and a two-dimensional navigator-based reacquisition, Magn. Reson. Med. 62 (2) (2009) 468–475.
[29] I. Tkac, Z. Starcuk, I.Y. Choi, R. Gruetter, In vivo 1H NMR spectroscopy of rat brain at 1 ms echo time, Magn. Reson. Med. 41 (4) (1999) 649–656.
[30] R. Gruetter, Automatic, localized in vivo adjustment of all first- and second-order shim coils, Magn. Reson. Med. 29 (6) (1993) 804–811.
[31] C. Juchem, C. Cudalbu, R.A. de Graaf, R. Gruetter, A. Henning, H.P. Hetherington, et al., B0 shimming for in vivo magnetic resonance spectroscopy: experts' consensus recommendations, NMR Biomed. 34 (5) (2021) e4350.
[32] S.W. Provencher, Estimation of metabolite concentrations from localized in vivo proton NMR spectra, Magn. Reson. Med. 30 (6) (1993) 672–679.
[33] M. Jenkinson, P. Bannister, M. Brady, S. Smith, Improved optimization for the robust and accurate linear registration and motion correction of brain images, Neuroimage 17 (2) (2002) 825–841.
[34] S.M. Smith, Fast robust automated brain extraction, Hum. Brain. Mapp. 17 (3) (2002) 143–155.
[35] M.W. Woolrich, B.D. Ripley, M. Brady, S.M. Smith, Temporal autocorrelation in univariate linear modeling of FMRI data, Neuroimage 14 (6) (2001) 1370–1386.
[36] K.J. Worsley, Statistical analysis of activation images, in: P Jezzard, PM Matthews, SM Smith (Eds.), Functional MRI: An Introduction to Methods, OUP, 2001.
[37] G.E. Zhou, Z.P. An, S. Gokhale, Moyamoya syndrome as an unusual presenting manifestation of systemic lupus erythematosus in a young woman, Med. Prin. Pract. 23 (3) (2014) 279–281.
[38] G. Hangel, S. Jain, E. Springer, E. Heckova, B. Strasser, M. Povazan, et al., High-resolution metabolic mapping of gliomas via patch-based super-resolution magnetic resonance spectroscopic imaging at 7T, Neuroimage 191 (2019) 587–595.
[39] Y. Li, P. Larson, A.P. Chen, J.M. Lupo, E. Ozhinsky, D. Kelley, et al., Short-echo three-dimensional H-1 MR spectroscopic imaging of patients with glioma at 7 Tesla for characterization of differences in metabolite levels, J. Magn. Reson. Imaging 41 (5) (2015) 1332–1341.
[40] C. Juchem, S.U. Rudrapatna, T.W. Nixon, R.A. de Graaf, Dynamic multi-coil technique (DYNAMITE) shimming for echo-planar imaging of the human brain at 7 Tesla, Neuroimage 105 (2015) 462–472.